

# Multiscale Modelling of Heterogeneous Structures Using Second-Order Computational Homogenization

<sup>1</sup>Faculty of Mechanical Engineering and Naval Architecture, University of Zagreb, Zagreb, Croatia

## Abstract

*A second-order two-scale computational homogenization procedure for modelling deformation responses of heterogeneous structures assuming small strains is presented. The macro-to-micro scale transition and generalized periodic boundary conditions on the representative volume element (RVE) are investigated. The macroscale is discretized by means of  $C^1$  two-dimensional triangular finite elements, while standard quadrilateral finite elements are used for the RVE discretization. The new proposed multiscale scheme has been implemented into the finite element software ABAQUS using user subroutine. The efficiency of the proposed multiscale homogenization approach is demonstrated by modelling of a pure bending problem.*

**Keywords:** multiscale analysis, heterogeneous materials, second-order homogenization,  $C^1$  finite element, periodic boundary conditions, Abaqus,

## 1. Introduction

In recent years, a special attention has been directed to investigation of mechanical properties of materials and their microstructure since almost all engineering materials can be treated as heterogeneous at some scale of observation. Since classical continuum mechanics does not consider structural effects in the material at the microlevels, a large number of multiscale techniques have been developed. In the multiscale procedure, the results obtained by the simulation of RVE, employing some of the homogenization methods, are used for the model at the macrolevel. To solve the microlevel boundary value problem, the finite element (FE) method is mostly used [1,2], but other methods are also available. A more detailed overview of development and application of the multiscale methods is presented in [3,4]. The computational homogenization method does not require an explicit a priori constitutive relation at the macrolevel. This makes its main advantage because it allows modelling of complex

microstructure geometry, arbitrary non-linear and time dependent material behaviour. Besides the computational homogenization, other homogenization methods are available, mostly developed before the computational homogenization, but in most cases, they are limited to a simple microstructure geometry and small strain constitutive models.

The results obtained by the homogenization, namely the tangent stiffness and the stress tensor depend on the boundary conditions (b. c.) applied on the RVE. Three most commonly used boundary conditions are prescribed displacements, prescribed tractions and periodicity conditions. Homogenization results obtained by prescribed displacements show too stiff homogenized RVE behaviour, while the RVE under traction boundary conditions exhibits too compliant homogenized behaviour. Periodic boundary conditions provide the best homogenization results and the fastest convergence properties by increasing RVE size. As shown in [5], the results obtained by the periodic boundary conditions lie between the values obtained by the prescribed displacements (upper bound), and the prescribed tractions (lower bound). However, periodic b. c. usually require regular RVE discretization on the edges where each node on independent edge must have a couple node on the dependent edge.

Based on the micro-macro variable dependence, first-order and the second-order homogenization procedures are available. Multiscale analysis using the first-order computational homogenization scheme allows explicit modelling of the microstructure, but retains local concept of the continuum mechanics, and gives satisfactory results only for the simple loading cases. It includes only the first gradient of the macroscopic displacement field and therefore, the size effects cannot be captured. Due to the mentioned shortcomings, first-order computational homogenization scheme has been extended to the second-order computational homogenization framework, where the second-order stress and strain are included. The formulation is based on a non-local continuum theory

which accounts for the influence of an environment on the behaviour of a material point [6,7]. Furthermore, the multiscale analysis using the second-order homogenization approach may describe more complex deformation modes. It requires a more complex formulation at the macrolevel ( $C^1$  continuity), which implicates the requirement that both displacements and deformations must be continuous functions. The microlevel in this case can remain standard keeping micro boundary value problem as simple as possible [8,9]. As well-known, to satisfy  $C^1$  continuity condition, the macrolevel model should be discretized by a higher-order finite element supporting additional degrees of freedom. But finite element formulations suited for nonlocal theory are rather complex and suffer from several drawbacks [10,11]. In addition, some formulations suffer from geometric restraints which may lead to incorrect results for second-order continuum problems. Therefore, for solving second-order continuum problems,  $C^0$  finite elements based on a mixed formulation have been developed in the last few years, where the displacements and displacement derivatives are considered as independent variables. Their kinematic relation is enforced by Lagrange multipliers [12] or by penalty functions [13].

An important problem in the second-order homogenization framework is definition of the scale transition methodology for the strains and strain gradients from the macroscale to the discretized microstructure. To establish a relation between the macro and micro variables, due to  $C^1$ - $C^0$  transition, there is a need for an alternative relation between the macrostrain gradient and the microstrain, which results in an additional integral condition on the fluctuation field at the microlevel [9]. There are several approaches to bridge a scale transition with account to the microfluctuation field. In [14], to establish a relation between the macroscopic gradient of the deformation gradient and the microscopic deformation gradient, an auxiliary integral relation has been considered. In integral, the microscopic gradient of the deformation gradient has a definition of a first moment of the deformation gradient. Also, the corner nodes fluctuations are fixed to zero, resulting in artificially stress concentrations. A more consistent approach is used in [15], where zero projection of the microfluctuations is enforced through orthogonality. On the other hand, the orthogonality is enforced by a vanishing surface integral of the micro-macro variable scalar product. But again, relaxed constraints on the fluctuation field are required to avoid corner stress

concentrations. In [16], a unified approach is proposed for the enforcement of the boundary conditions using multiple constraint projection matrices. To preserve the classical microstructural boundary value problem, an assumption of the second moment of deformed RVE area has been performed, resulting in similar integral constraint as in [9]. In [17], the micro displacement field is composed of two components, the local macroscopic displacements and the microfluctuations. The unknown fluctuation field is composed of two unknown functions, related to the first-order and the second-order strain, respectively. However, due to the mathematically rigorous and computationally expensive procedure, this tool is only appropriate for periodic microstructures.

The paper presents the multiscale algorithm using the second-order computational homogenization for a small strain case. A special attention is directed to the application of the generalized periodic boundary conditions on the representative volume element (RVE). Besides the generalized periodic boundary conditions, the displacement b. c. are also derived. The macrolevel is discretized by a two-dimensional  $C^1$  triangular finite element, reformulated to the requirements of the second-order computational homogenization from the original formulation for the plate bending problems [18]. The discretization at microlevel is performed using the standard quadrilateral finite elements for plane strain conditions. A computational strategy for the implementation of the imposed integral conditions on the RVE boundary is proposed. All numerical algorithms derived are implemented into FE software ABAQUS [19] using user subroutines. The performance of the proposed formulations is demonstrated by the numerical examples.

The paper is organized as follows. Section 2 briefly discusses the formulation and numerical implementation of the  $C^1$  triangular finite element. In Section 3 the basic relations of a multiscale algorithm with the second-order computational homogenization are derived. The presented multiscale algorithm has been verified on a pure bending problem. Finally, some concluding remarks are given in the last section.

## 2. 2D $C^1$ triangular finite element

### *Strain gradient continuum formulation*

The basic strain gradient continuum relations are thoroughly discussed in [9,20]. For two-dimensional problems considered here Latin indices take the values 1

and 2.  $\sigma_{ij}$  and  $\mu_{kij}$  are the stress tensor and the second-order (double stress) tensor, respectively. An energy conjugate to the stress tensor is the strain tensor represented by  $\varepsilon_{ij} = \frac{1}{2}(u_{i,j} + u_{j,i})$  with  $u_i$  defined as the displacement vector. An energy conjugate to the double stress is a third-order strain gradient tensor  $\varepsilon_{ij,k} \cdot t_i$  and  $\tau_i$  are the traction and the double surface traction, respectively. Using the principle of virtual work, ( $\delta W_I = \delta W_E$ ), yields the equilibrium equation

$$\sigma_{ij,j} - \mu_{kji,kj} = 0. \quad (1)$$

### Finite element implementation

The relations of nonlocal continuum theory have been implemented into the  $C^1$  triangular finite element shown in Fig. 1. The element has three nodes, each with twelve degrees of freedom (DOF). The nodal degrees of freedom are the two displacements and their first and second order derivatives with respect to the Cartesian coordinates. The element is called C1PE3, describing  $C^1$  continuity and plane strain state. The element displacement field is approximated by the condensed fifth order polynomial. More precisely, 21 coefficients are required for a complete polynomial, but by means of the element degrees of freedom, only 18 equations can be defined. An additional three equations are obtained from the condition that the normal derivative of displacement along the element edge is constrained to vary as a cubic polynomial.

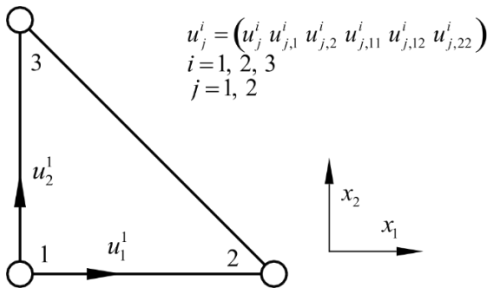


Fig. 1.  $C^1$  triangular finite element

As usually, the element equations are derived from the variation of the principle of virtual work, which may be expressed for strain gradient continuum as

$$\int_A \delta \boldsymbol{\varepsilon}^T \boldsymbol{\sigma} dA + \int_A \delta \boldsymbol{\eta}^T \boldsymbol{\mu} dA = \int_s \delta \mathbf{u}^T \mathbf{t} ds + \int_s \delta (\text{grad } \mathbf{u}^T) \mathbf{T} ds. \quad (2)$$

In Eq. (2),  $\boldsymbol{\sigma}$  and  $\boldsymbol{\varepsilon}$  are the stress and strain tensors, respectively.  $\boldsymbol{\eta}$  represents the second-order strain tensor

containing appropriate second derivatives of the displacement vector  $\mathbf{u}$ , while  $\mathbf{T}$  is the double traction tensor,  $\mathbf{T} = \boldsymbol{\tau} \mathbf{n}$ .  $A$  and  $s$  represent area and perimeter of the triangle, respectively. The displacement gradients can be derived as

$$\boldsymbol{\varepsilon} = \begin{bmatrix} \varepsilon_{11} \\ \varepsilon_{22} \\ 2\varepsilon_{12} \end{bmatrix} = \mathbf{B}_\varepsilon \mathbf{v}, \boldsymbol{\eta} = \begin{bmatrix} \eta_{111} \\ \eta_{222} \\ \eta_{221} \\ \eta_{122} \\ 2\eta_{121} \\ 2\eta_{212} \end{bmatrix} = \mathbf{B}_\eta \mathbf{v}, \quad (3)$$

where  $\mathbf{B}_\varepsilon$  and  $\mathbf{B}_\eta$  are the matrices containing corresponding the first and second derivatives of the interpolation functions  $\mathbf{N}$ , and  $\mathbf{v}$  represents the vector of nodal degrees of freedom. For nonlinear problems, Eq. (2) is linearized in the time interval  $(t^{i-1}, t)$ , where  $t^{i-1}$  represents the time increment of the last converged equilibrium state, and  $t$  is the new affine state obtained in the iterative procedure by updates

$$\begin{aligned} \mathbf{u} &= \mathbf{u}^{i-1} + \Delta \mathbf{u}, \\ \boldsymbol{\sigma} &= \boldsymbol{\sigma}^{i-1} + \Delta \boldsymbol{\sigma}, \\ \boldsymbol{\mu} &= \boldsymbol{\mu}^{i-1} + \Delta \boldsymbol{\mu}. \end{aligned} \quad (4)$$

The increments of the stress  $\Delta \boldsymbol{\sigma}$  and the second-order stress  $\Delta \boldsymbol{\mu}$  are computed assuming the generalized constitutive relations

$$\begin{aligned} \Delta \boldsymbol{\sigma} &= \mathbf{C}_{\sigma\varepsilon} \Delta \boldsymbol{\varepsilon} + \mathbf{C}_{\sigma\eta} \Delta \boldsymbol{\eta}, \\ \Delta \boldsymbol{\mu} &= \mathbf{C}_{\mu\varepsilon} \Delta \boldsymbol{\varepsilon} + \mathbf{C}_{\mu\eta} \Delta \boldsymbol{\eta}. \end{aligned} \quad (5)$$

In Eq. (5),  $\mathbf{C}_{\sigma\varepsilon}$ ,  $\mathbf{C}_{\sigma\eta}$ ,  $\mathbf{C}_{\mu\varepsilon}$  and  $\mathbf{C}_{\mu\eta}$  are the material tangent stiffness matrices. By means of standard manipulations in the finite element method, which is also explained in [9] the standard finite element equation is obtained

$$\mathbf{K} \Delta \mathbf{v} = \mathbf{F}_e - \mathbf{F}_i. \quad (6)$$

In Eq. (6), stiffness matrix is expressed as

$$\mathbf{K} = \mathbf{K}_{\sigma\varepsilon} + \mathbf{K}_{\sigma\eta} + \mathbf{K}_{\mu\varepsilon} + \mathbf{K}_{\mu\eta}, \quad (7)$$

where the particular submatrices are

$$\begin{aligned} \mathbf{K}_{\sigma\varepsilon} &= \int_A (\mathbf{B}_\varepsilon^T \mathbf{C}_{\sigma\varepsilon} \mathbf{B}_\varepsilon) dA, \quad \mathbf{K}_{\sigma\eta} = \int_A (\mathbf{B}_\varepsilon^T \mathbf{C}_{\sigma\eta} \mathbf{B}_\eta) dA, \\ \mathbf{K}_{\mu\varepsilon} &= \int_A (\mathbf{B}_\eta^T \mathbf{C}_{\mu\varepsilon} \mathbf{B}_\varepsilon) dA, \quad \mathbf{K}_{\mu\eta} = \int_A (\mathbf{B}_\eta^T \mathbf{C}_{\mu\eta} \mathbf{B}_\eta) dA. \end{aligned} \quad (8)$$

Furthermore,  $\mathbf{F}_e$  and  $\mathbf{F}_i$  are the external and internal nodal force vectors, expressed as

$$\begin{aligned} \mathbf{F}_e &= \int_s (\mathbf{N}^T \mathbf{t} + \text{grad} \mathbf{N}^T \mathbf{T}) ds, \\ \mathbf{F}_i &= \int_A (\mathbf{B}_\varepsilon^T \boldsymbol{\sigma}^{i-1} + \mathbf{B}_\eta^T \boldsymbol{\mu}^{i-1}) dA. \end{aligned} \quad (9)$$

The element has been implemented into the FE program ABAQUS using the user element subroutine UEL. Using Gauss numerical integration method, stiffness matrix of the C1PE3 element requires 25 points in full integration scheme. To increase numerical efficiency of the multiscale scheme, the reduced integration technique with 13 integration points is used. By reduced integration procedure satisfactory results are provided, without introduction of additional rigid body (zero energy) modes.

### 3. Scale transition algorithm

The micro-macro algorithm consists of the two models representing two different levels. The first level represents the macromodel. The second level (microstructure) is presented by the representative volume element. In the text that follows the macroscopic quantities are denoted by the subscript ‘‘M’’, while the microscopic values are labeled with the subscript ‘‘m’’. In every macrolevel integration point of the structural mesh, the RVE microanalysis is performed. The macrolevel displacement gradients  $\boldsymbol{\varepsilon}_M$  and  $\boldsymbol{\eta}_M$  are transformed into the RVE boundary nodal displacements using corresponding boundary conditions. After solving the RVE boundary value problem, the stress  $\boldsymbol{\sigma}_M$ , the double stress  $\boldsymbol{\mu}_M$  and the constitutive matrices  $\mathbf{C}_M$  are obtained by a homogenization procedure. The general scheme of the micro-macro algorithm is presented in Fig. 2 and detailed in [9].

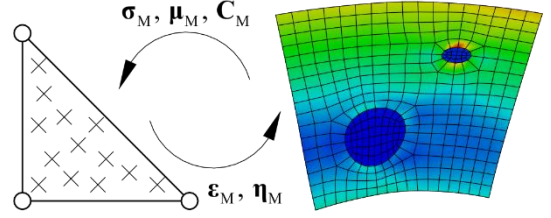


**Fig. 2.** Scheme of the micro-macro algorithm

In the second-order homogenization the RVE displacement field is obtained by Taylor expansion series as

$$\mathbf{u}_m = \boldsymbol{\varepsilon}_M \mathbf{x} + \frac{1}{2} \mathbf{x}^T \boldsymbol{\eta}_M \mathbf{x} + \mathbf{r} \quad (10)$$

with  $\mathbf{x}$  as spatial coordinate on the RVE boundary, and  $\mathbf{r}$  representing the microstructural fluctuation field, i.e., the microlevel contribution to the RVE displacement field. The volume average of the microstrain, based on Eq. (10) is expressed as

$$\frac{1}{V} \int_V \boldsymbol{\varepsilon}_m dV = \boldsymbol{\varepsilon}_M + \frac{1}{V} \int_V (\boldsymbol{\eta}_M \mathbf{x}) dV + \frac{1}{V} \int_V \text{grad} \mathbf{r} dV, \quad (11)$$

where  $V$  represents the RVE volume. To satisfy averaging principles, the second and third terms in the right-hand side of (11) should vanish. By setting the coordinate system origin into the RVE centroid (Fig. 3), the second term is eliminated. The third term must be explicitly imposed

$$\frac{1}{V} \int_V \text{grad} \mathbf{r} dV = \frac{1}{V} \int_A (\mathbf{n} \mathbf{r}) dA = \mathbf{0}. \quad (12)$$

The second order strain at the microlevel  $\boldsymbol{\eta}_m$  is assumed in the form

$$\boldsymbol{\eta}_m = \int_V (\boldsymbol{\varepsilon}_m \mathbf{x} + \mathbf{x}^T \boldsymbol{\varepsilon}_m) dV, \quad (13)$$

according to [9,14]. Inserting of (11) into (13), and after a lengthy procedure gives an additional integral constraint

$$\int_A (\mathbf{n}^T \mathbf{r} \mathbf{x} + \mathbf{x}^T \mathbf{r} \mathbf{n}) dA = \mathbf{0}. \quad (14)$$

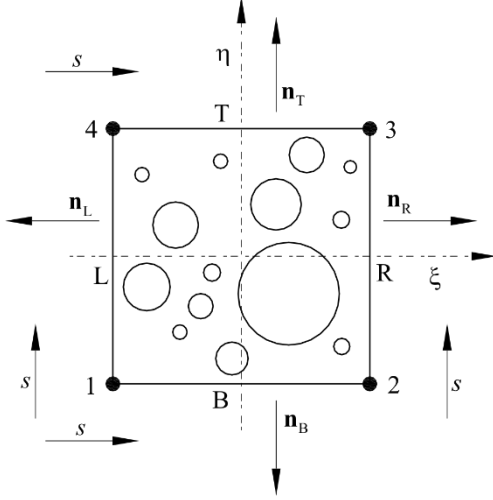


**Fig. 3.** Representative volume element

The RVE boundary conditions must satisfy constraints (12) and (14). The displacement boundary conditions obey the assumption that  $\mathbf{r} = \mathbf{0}, \forall \mathbf{x} \in \partial V$ , which yields the satisfaction of the two aforementioned relations. The generalized periodic boundary conditions assume identical microfluctuation field on the opposite RVE sides in form

$$\begin{aligned} \mathbf{r}_L(s) &= \mathbf{r}_R(s), \\ \mathbf{r}_T(s) &= \mathbf{r}_B(s), \end{aligned} \quad (15)$$

where  $s$  is a local coordinate along the edges L, R, T and B standing for the left, right, top and bottom RVE edges. Considering periodicity (15), to satisfy constraint (14) two additional equations must be prescribed on the independent edges, e.g. left and bottom using Eq. (10), which leads to

$$\begin{aligned} \int_{A_L} \mathbf{u}_L dA &= \boldsymbol{\varepsilon}_M \int_{A_L} \mathbf{x}_L dA + \frac{1}{2} \boldsymbol{\eta}_M \int_{A_L} (\mathbf{x}_L^T \mathbf{x}_L) dA, \\ \int_{A_B} \mathbf{u}_B dA &= \boldsymbol{\varepsilon}_M \int_{A_B} \mathbf{x}_B dA + \frac{1}{2} \boldsymbol{\eta}_M \int_{A_B} (\mathbf{x}_B^T \mathbf{x}_B) dA. \end{aligned} \quad (16)$$

Homogenization of the stress is conducted according to the Hill-Mandel condition

$$\frac{1}{V} \int_V (\boldsymbol{\sigma}_m : \delta \boldsymbol{\varepsilon}_m) dV = \boldsymbol{\sigma}_M : \delta \boldsymbol{\varepsilon}_M + \boldsymbol{\mu}_M : \delta \boldsymbol{\eta}_M. \quad (17)$$

By means of Eq. (17), the homogenized stress tensors can be derived

$$\begin{aligned} \boldsymbol{\sigma}_M &= \frac{1}{V} \int_V \boldsymbol{\sigma} dV = \frac{1}{V} \mathbf{D} \mathbf{f}_b, \\ \boldsymbol{\mu}_M &= \frac{1}{2V} \int_V (\boldsymbol{\sigma}_m^T \mathbf{x} + \mathbf{x}^T \boldsymbol{\sigma}_m) dV = \frac{1}{V} \mathbf{H} \mathbf{f}_b. \end{aligned} \quad (18)$$

In Eqs. (18), the matrices  $\mathbf{D}$  and  $\mathbf{H}$ , are the coordinate matrices involving all the boundary nodes of the RVE, and  $\mathbf{f}_b$  is a vector of boundary RVE nodal forces [9,16]. To obtain homogenized constitutive behaviour as assumed in Eq. (5), static condensation procedure is employed. By this global RVE stiffness matrix is expressed only by the contributions of the external nodes

$$\tilde{\mathbf{K}}_{bb} = \mathbf{K}_{bb} - \mathbf{K}_{ba} \mathbf{K}_{aa}^{-1} \mathbf{K}_{ab} \quad (19)$$

as described in [9].  $\mathbf{K}_{aa}$ ,  $\mathbf{K}_{ab}$ ,  $\mathbf{K}_{ba}$  and  $\mathbf{K}_{bb}$  are the global RVE stiffness submatrices obtained by means of the topological projection matrices, defining internal and boundary contributions. After some straightforward calculus the constitutive operators can be extracted from the RVE in the form

$$\begin{aligned} \mathbf{C}_{\sigma\varepsilon} &= \frac{1}{V} \mathbf{D} \tilde{\mathbf{K}}_{bb} \mathbf{D}^T, \quad \mathbf{C}_{\sigma\eta} = \frac{1}{V} \mathbf{D} \tilde{\mathbf{K}}_{bb} \mathbf{H}^T, \\ \mathbf{C}_{\mu\varepsilon} &= \frac{1}{V} \mathbf{H} \tilde{\mathbf{K}}_{bb} \mathbf{D}^T, \quad \mathbf{C}_{\mu\eta} = \frac{1}{V} \mathbf{H} \tilde{\mathbf{K}}_{bb} \mathbf{H}^T. \end{aligned} \quad (20)$$

#### 4. Numerical example

A rectangular strip of the length and height of 0.2 m and thickness 1 m subjected to bending is considered. The deformation response of a square model discretized by 16 plane strain triangular finite elements is studied, as shown in Fig. 4. The imposed loading and boundary conditions reproduce the deformed configuration of the macro model displaying constant curvature. The material considered is an academic example of a steel with porous microstructure. The material data are the Young's modulus  $E = 210\text{GPa}$ , the Poisson's ratio  $\nu = 0.3$ , the yield stress of 250 MPa and the elastoplastic tangent modulus of 250 MPa describing isotropic hardening. Two RVEs with the porosities of 13% and 27% randomly distributed voids are analysed, as presented in Fig. 5. The side length of the RVEs is taken 0.2 mm. For the sake of comparison, the homogeneous structure is also considered. The microlevel discretization with 13% voids of the average radius of 0.043 mm is performed by 508 quadrilateral finite elements, while the discretization of the RVE with 27% voids of the average radius of 0.0086 mm is carried out using 1198 quadrilateral elements.

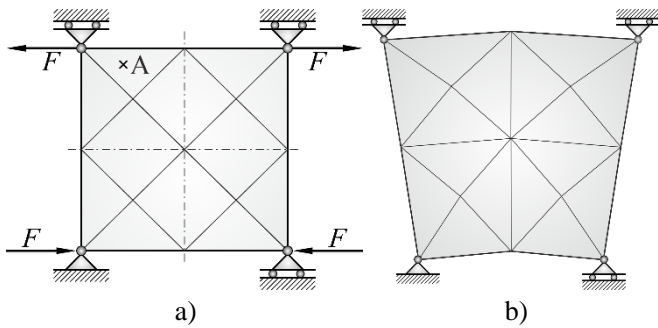


**Fig. 4.** Pure bending problem: a) discretization and loading, b) deformed configuration

The moment-curvature diagram presenting the deformation responses for the two different computational variants is shown in Fig. 6. The diagram displays that the stiffness of the analysed specimens is significantly decreased when the material porosity is increased from 13% to 27 %, as expected. Accordingly, for the same curvature the bending moment is significantly reduced if the porosity is increased. It should be stressed that the computational results display the realistic structural behaviour, which demonstrates the accuracy of the proposed computational algorithms.

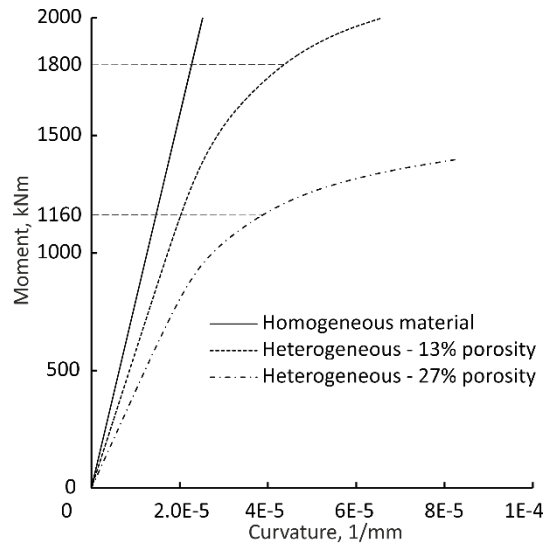


**Fig. 6.** Moment-curvature diagram

The distribution of the effective plastic strain over the deformed RVEs at the integration point A shown in Fig. 4, for the two different bending moments, which are associated to different curvatures, for the porosities displayed in Fig. 5 are presented in Figs. 7 and 8.

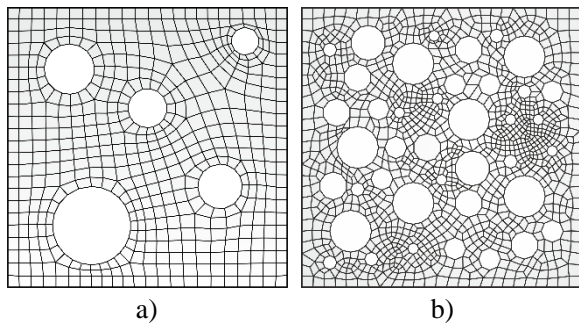


**Fig. 5.** Representative volume elements with a) 13% voids, b) 27% voids

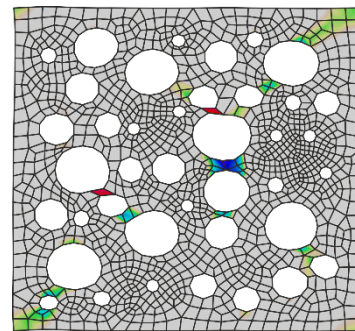


**Fig. 7.** Distribution of effective plastic strain over RVE at integration point A for bending moment of 1160 kNm and porosity of 27%

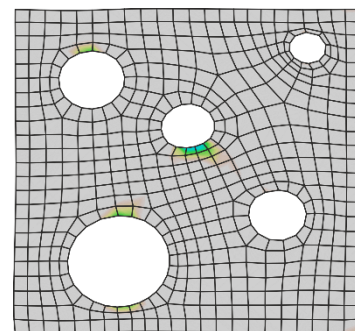


**Fig. 8.** Distribution of effective plastic strain over RVE at integration point A for bending moment of 1800 kNm and porosity of 13%

It is obvious in Fig. 6 that the structure consisting of the material with the 13% of porosity remains in the elastic range at the bending moment of 1160 kNm, while a nonlinear response is displayed in the case of 27% voids. For the larger porosity Fig. 7 shows that the microstructural shear bands between voids are developed in. At the bending moment of 1800 kNm, the plastic zones occur only in the small local domains around the voids in the material with 13% porosity. It can be observed that the deformed RVEs are not able to demonstrate the macroscopic deformation pattern because of very large ratio between the microscopic and macroscopic side lengths. The microscopic curvature would be more pronounced, if a larger RVE size has been used. It is known that the determination of the RVE represents an important issue in the homogenization concept. This is particularly important in the second-order homogenization approach, where the nonlocal influence is in direct correlation to the RVE size. However, the RVE determination and its influence on the structural responses is beyond the scope of this paper.

## 5. Conclusions

A micro-macro computational strategy employing the second-order computational homogenization scheme for heterogeneous materials at small strains has been presented. According to the second-order formulation, the macrolevel is discretized by the  $C^1$  plane strain triangular finite element based on the strain gradient theory, while the standard  $C^0$  quadrilateral finite element is used for the discretization at the microlevel. The  $C^1$  element derived for nonlinear analysis is implemented into the FE software ABAQUS by means of the user-defined subroutine UEL. In the frame of the second-order computational homogenization, issues related to the application of the boundary conditions on the representative volume element at the microlevel are discussed. Herein, both the displacement and the generalized periodic boundary conditions are considered. The new proposed multiscale computational strategy has been again implemented into the ABAQUS via user subroutines UEL at the macrolevel, and via UELMAT at the microlevel. For imposition of the microfluctuation constraint it has been demonstrated in [9] that trapezoidal rule gives a physically correct deformation response.

Efficiency and accuracy of the proposed multiscale approach is demonstrated by a typical numerical example in multiscale analysis, the pure bending problem. The realistic deformation responses of the models at both scales demonstrate the accuracy of the proposed computational approach.

## References

- [1] Brekelmans, W.A.M., Geers, M.G.D., Kouznetsova, V.G., Computational Homogenisation for Non-Linear Heterogeneous Solids. In: *Multiscale Modeling in Solid Mechanics*, 1–42 (2009).
- [2] Nguyen, V.D., Becker, G., Noels, L., Multiscale computational homogenization methods with a gradient enhanced scheme based on the discontinuous Galerkin formulation. *Comput Methods Appl Mech Eng.*, 260, 63–77 (2013).
- [3] Matouš, K., Geers, M.G.D., Kouznetsova, V.G., Gillman, A., A review of predictive nonlinear theories for multiscale modeling of heterogeneous materials. *Mechanics of Materials*, 330, 192–220 (2017).
- [4] Geers, M.G.D., Kouznetsova, V.G., Brekelmans, W.A.M., Multi-scale computational homogenization: Trends and challenges, *J Comput Appl Math.*, 234(7), 2175–2182 (2010).
- [5] Miehe, C., Koch, A., Computational micro-to-macro transitions of discretized microstructures undergoing small strains. *Arch Appl Mech.*, 72(4–5), 300–317 (2002).
- [6] Mindlin, R.D., Second gradient of strain and surface-tension in linear elasticity. *Int J Solids Struct.*, 1(4), 417–438 (1965).
- [7] Toupin, R.A., Theories of elasticity with couple-stress. *Arch Ration Mech Anal.*, 17(2), 85–112 (1964).
- [8] Kouznetsova, V.G., Geers, M.G.D., Brekelmans, W.A.M., Multi-scale second-order computational homogenization of multi-phase materials: a nested finite element solution strategy, *Comput Methods Appl Mech Eng.*, 193, 5525–50 (2004).
- [9] Lesičar, T., Tonković, Z., Sorić, J., A second-order two-scale homogenization procedure using  $C^1$  macrolevel discretization. *Comput Mech.*, 54(2), 425–441 (2014).
- [10] Petera, J., Pittman, J.F.T., Isoparametric Hermite elements. *Int J Numer Methods Eng.*, 37(20), 3489–3519 (1994).
- [11] Zervos, A., Papanastasiou, P., Vardoulakis, I., Modelling of localisation and scale effect in thick-walled cylinders with gradient elastoplasticity. *Int J Solids Struct.*, 38(30–31), 5081–95 (2001).
- [12] Amanatidou, E., Aravas, N., Mixed finite element formulations of strain-gradient elasticity problems. *Comput Methods Appl Mech Eng.*, 191, (1723–51)

(2002).

- [13] Zervos, A., Papanicolopoulos, S., Vardoulakis, I., Two Finite-Element Discretizations for Gradient Elasticity. *J Eng Mech.*, 135(3), 203–13 (2009).
- [14] Kouznetsova, V.G., Geers, M., Brekelmans, W.A.M., Size of a Representative Volume Element in a Second-Order Computational Homogenization Framework. *Int J Multiscale Comput Eng.*, 2(4), 24 (2004).
- [15] Luscher, D., McDowell, D., Bronkhorst, C., Essential Features of Fine Scale Boundary Conditions for Second Gradient Multiscale Homogenization of Statistical Volume Elements. 10(5), 461–86 (2012).
- [16] Kaczmarczyk, L.K., Pearce, C.J., Bicanic, N., Scale transition and enforcement of RVE boundary conditions in second-order computational homogenization. *Int J Numer Methods Eng.*, 74(3), 506–22, 2008.
- [17] Bacigalupo, A., Gambarotta, L., Second-order computational homogenization of heterogeneous materials with periodic microstructure. *ZAMM - J Appl Math Mech / Zeitschrift für Angew Math und Mech.*, 90(10–11), 796–811, (2010).
- [18] Dasgupta, S., Sengupta, D., A higher-order triangular plate bending element revisited. *Int J Numer Methods Eng.*, 30(3), 419–30 (1990).
- [19] Abaqus 6.14-1, Dassault Systemes Simulia Corp., Providence, RI, USA, 2014.
- [20] Lesičar, T., Tonković, Z., Sorić, J., Two-scale computational approach using strain gradient theory at microlevel. *Int J Mech Sci.*, 126, 67-78 (2017).